Monolithic Waveguide Filters Using Printed Photonic-Bandgap Materials

Chryssoula A. Kyriazidou, *Member, IEEE*, Harry F. Contopanagos, *Member, IEEE*, and
Nicólaos G. Alexópoulos, *Fellow, IEEE*

***Abstract*—A system of N dielectric layers imprinted with a transverse lattice of planar metallic scatterers and stacked monolithically along the longitudinal direction of a rectangular waveguide is examined in this paper. This monolithically constructed photonic crystal exhibits valuable filtering properties. The resulting optimized filters are inexpensive to fabricate because the building block (printed layer) is ideal for mass production. The complete filter contains no air gaps (monolithic) and can be modularly built up, or reconfigured, by simple stacking requiring no adhesives (modular). The filter response is designed using our analytical expressions and fast software, as well as using commercial software such as HFSS. A comparison of the two design methods shows that our approach is five orders of magnitude faster than HFSS and significantly reduces the memory requirements. Prototype measurements in the Ka-band show excellent agreement with predictions of our design method. Optimized designs displaying reduced size, extremely flat passbands (0.25 dB), and great isolation (-100 dB) are also presented.**

***Index Terms*—Filter, photonic-bandgap material, waveguide.**

I. INTRODUCTION

TRADITIONAL microwave waveguide filters are based on a lumped-element analysis and optimization [1]–[3]. The analysis presupposes individual scatterers localized inside the waveguide volume. A transmission line is built up of scatterers that are sufficiently spread out so that higher order scattering modes do not interact. The corresponding lumped description of the scattering can be successfully translated into higher frequencies through transmission-line theory. Close spacing of the individual scatterers implies higher mode coupling, resulting in evanescent mode filters that exhibit smaller size, broader bandwidth, and low loss [4]–[6]. Recently, single and coupled resonators have been analyzed rigorously in terms of a full-wave electromagnetic (EM) approach [7]–[11]. Practical realizations involve scattering discontinuities like posts, metallic irises, or dielectric elements.

While traditional design procedures are very robust, if the localized scatterer is of appropriate (small) electrical size, they usually require successive scatterers to be spread out along the propagation direction. Further, since the scatterers are not always symmetric on the transverse plane, each filter section produces ripple in the passbands, which can be suppressed with a considerable number of sections, and these circumstances result in large filter lengths. This traditional approach excludes the analysis of scatterers that are embedded symmetrically along the transverse guide plane, within a high-permittivity host dielectric [12], [13]. These configurations however, may have interesting and competitive filtering properties that might produce better and more compact filters, and this is the motivation of this paper.

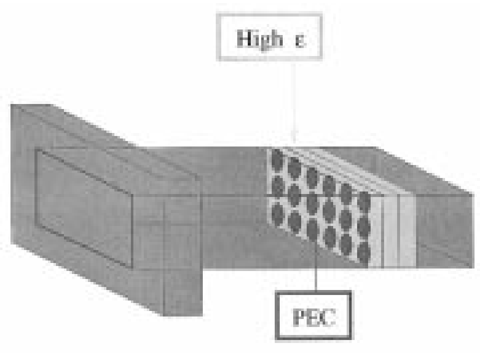

Fig. 1. Printed metalodielectric PBG filter press fit in a rectangular waveguide.

In this paper, we propose a novel filter architecture, where the basic building block of the filter is a dielectric layer printed with a periodic two-dimensional (2-D) lattice of planar metallic scatterers. The resulting layer is then press fit inside the waveguide, or framed within a conformal metallic bezel, as shown in Fig. 1. This insertion, even though physically representing a finite lattice composed of few printed elements, is electromagnetically equivalent to an infinite transverse lattice, due to the reflections on the guide wall. To be conformal with these reflections, we will only examine orthogonal transverse lattices, cut along symmetry planes only. The basic building block is, therefore, equivalent to a 2-D photonic crystal, or photonic bandgap (PBG) material [14], [15]. Reconstruction of the filter in the z-direction is achieved through transfer-matrix analysis.

The organization of this paper is as follows. In Section II, we present formulas that reduce the calculation of the filter response under waveguide excitations to that of plane waves. In Section III, an analytical calculation of the printed multilayer response in terms of the shunt susceptance of a single embedded planar array of printed elements is presented, including high-frequency radiative corrections to the Bethe small-hole theory. The calculation is valid for an arbitrary number N of printed layers, inside the guide walls, for any TE_{nm} and TM_{nm} modes.

Manuscript received August 10, 1999.

C. A. Kyriazidou is with the Department of Electrical Engineering, University of California at Los Angeles, Los Angeles, CA 90095 USA (e-mail: kyria@ee.ucla.edu).

H. F. Contopanagos was with the Department of Electrical and Computer Engineering, University of California Irvine, Irvine, CA 92697 USA. He is now with HRL Laboratories, Malibu, CA 90265 USA (e-mail: contopan@hrl.com).

N. G. Alexópoulos is with the Department of Electrical and Computer Engineering, University of California at Irvine, Irvine, CA 92697 USA (e-mail: alfios@uci.edu).

Publisher Item Identifier S 0018-9480(01)01069-9.

The corresponding design formulas are fully analytical and require negligible computer time to produce predictions (typically 10^3 data points/real seconds on an HP workstation). The performance of our approach is compared with the multiple frequency-sweep runs of commercial codes like HFSS, where each run lasts typically 8–10 h, producing just one resonance in a multiply resonant frequency range. In Section IV, we describe our experiments, using nonoptimized designs in order to both, validate our approach, and show the general characteristics of the filter response under TE_{10} excitation. The measurements are in excellent agreement with our analytical theory. We further show the theoretical response of an optimized filter configuration, designed for a flat-passband TE_{10}-mode filter. We achieve deep isolation and extremely flat passbands, including realistic material loss. We further provide HFSS simulations of the optimized filter response, which also are in excellent agreement with our analytical treatment. Finally, in Section IV, we summarize our conclusions and point out that this system is also suited for harmonic extraction or rejection of higher modes within their propagating bands.

II. WAVEGUIDE FILTER RESPONSE DERIVED FROM PLANE-WAVE INCIDENCE

Given that the building block of our filter is a transverse printed lattice of infinite extent (due to the images), immersed in a homogeneous dielectric, its EM response under any guide mode excitation can be derived through the corresponding response for plane-wave incidence. This approach automatically satisfies energy conservation and, therefore, avoids the subtle complications arising from a network approach. We demonstrate this for all TE modes.

The TE_{nm} guide modes normalized to an arbitrary constant may be written as

$$\mathbf{E}_{nm} = \hat{\mathbf{x}} E_{nm}^{x} + \hat{\mathbf{y}} E_{nm}^{y} \tag{1}$$

where

$$\begin{aligned} E_{nm}^{x} &= 4jC_{nm} k_m \cos(k_n x)\sin(k_m y) e^{-\gamma_{nm} z} \\ E_{nm}^{y} &= -4jC_{nm} k_n \sin(k_n x)\cos(k_m y) e^{-\gamma_{nm} z} \end{aligned} \tag{2}$$

where

$$\begin{aligned} k_n &\equiv \frac{n\pi}{a} \\ k_m &\equiv \frac{m\pi}{b} \\ 4C_{nm} &\equiv \frac{k_0 Z_0}{k_{nm}^2} \\ k_{nm}^2 &\equiv k_n^2 + k_m^2 \\ \gamma_{nm} &\equiv j\beta_{nm} = j\sqrt{k_0^2 - k_{nm}^2}. \end{aligned} \tag{3}$$

The modes in (1)–(3) can be written as the plane-wave superposition

$$\mathbf{E}_{nm} = C_{nm} \sum_{i=1}^{4} \hat{\mathbf{p}}_{nm}^{(i)} \exp\left(-jk_0 \hat{\mathbf{k}}_{nm}^{(i)} \cdot \mathbf{r}\right) \tag{4}$$

where the unit polarization vectors $\hat{\mathbf{p}}_{nm}^{(i)}$ and unit wave vectors $\hat{\mathbf{k}}_{nm}^{(i)}$ are given as

$$\begin{aligned} \hat{\mathbf{p}}_{nm}^{(1)} &= \cos(\phi_{nm})\hat{\mathbf{x}} + \sin(\phi_{nm})\hat{\mathbf{y}} \\ \hat{\mathbf{k}}_{nm}^{(1)} &= \sin(\theta_{nm})\sin(\phi_{nm})\hat{\mathbf{x}} - \sin(\theta_{nm})\cos(\phi_{nm})\hat{\mathbf{y}} \\ &\quad + \cos(\theta_{nm})\hat{\mathbf{z}} \\ \hat{\mathbf{p}}_{nm}^{(2)} &= -\cos(\phi_{nm})\hat{\mathbf{x}} - \sin(\phi_{nm})\hat{\mathbf{y}} \\ \hat{\mathbf{k}}_{nm}^{(2)} &= -\sin(\theta_{nm})\sin(\phi_{nm})\hat{\mathbf{x}} + \sin(\theta_{nm})\cos(\phi_{nm})\hat{\mathbf{y}} \\ &\quad + \cos(\theta_{nm})\hat{\mathbf{z}} \\ \hat{\mathbf{p}}_{nm}^{(3)} &= \cos(\phi_{nm})\hat{\mathbf{x}} - \sin(\phi_{nm})\hat{\mathbf{y}} \\ \hat{\mathbf{k}}_{nm}^{(3)} &= -\sin(\theta_{nm})\sin(\phi_{nm})\hat{\mathbf{x}} - \sin(\theta_{nm})\cos(\phi_{nm})\hat{\mathbf{y}} \\ &\quad + \cos(\theta_{nm})\hat{\mathbf{z}} \\ \hat{\mathbf{p}}_{nm}^{(4)} &= -\cos(\phi_{nm})\hat{\mathbf{x}} + \sin(\phi_{nm})\hat{\mathbf{y}} \\ \hat{\mathbf{k}}_{nm}^{(4)} &= \sin(\theta_{nm})\sin(\phi_{nm})\hat{\mathbf{x}} + \sin(\theta_{nm})\cos(\phi_{nm})\hat{\mathbf{y}} \\ &\quad + \cos(\theta_{nm})\hat{\mathbf{z}} \end{aligned} \tag{5}$$

and the spherical angles are given by

$$\sin(\theta_{nm}) = \frac{k_{nm}}{k_0} \qquad \sin(\phi_{nm}) = \frac{k_m}{k_{nm}}. \tag{6}$$

Notice in (5) that the polarization pairs $\hat{\mathbf{p}}_{nm}^{(1)}, \hat{\mathbf{p}}_{nm}^{(2)}$, and $\hat{\mathbf{p}}_{nm}^{(3)}, \hat{\mathbf{p}}_{nm}^{(4)}$ are antiparallel, while all four partial waves are transverse, i.e., $\hat{\mathbf{p}}_{nm}^{(i)} \cdot \hat{\mathbf{k}}_{nm}^{(i)} = 0$.

For single-index TE modes ($m = 0$), the polar angle $\phi_{nm} = 0$ and the plane of incidence of the plane waves in (4) is oriented along the symmetry planes of the photonic crystal. Further, the reflection and transmission coefficients are also invariant under $\theta_{nm} \leftrightarrow -\theta_{nm}$. Hence, all plane waves in (4) have a common reflection and transmission coefficient, which are the same as those of a TE-polarized plane wave under incidence angle θ_{nm}, i.e.,

$$\Gamma_{nm}^{\mathrm{TE}} = \Gamma^{\mathrm{TE}}(\theta_{nm}), quad T_{nm}^{\mathrm{TE}} = T^{\mathrm{TE}}(\theta_{nm}). \tag{7}$$

Strictly speaking, this result does not hold for double-index modes ($n, m \neq 0$) because then $\phi_{nm} \neq 0$ and the corresponding plane of incidence is tilted with respect to the x–z-plane, which is a symmetry plane of the photonic crystal. In that case, partial-wave analysis of the incident plane waves into a component set respecting the symmetry has to be performed first. Practically, conclusions based on (7) will still be valid for these modes provided the transverse lattice and printed element size are small enough so that the lattice interaction constants are negligible. In this paper, we only examine the dominant TE_{10} mode and, therefore, we will not elaborate on this point further.

A similar result holds for the TM_{nm} modes, i.e.,

$$\Gamma_{nm}^{\mathrm{TM}} = \Gamma^{\mathrm{TM}}(\theta_{nm}) \quad T_{nm}^{\mathrm{TM}} = T^{\mathrm{TM}}(\theta_{nm}). \tag{8}$$

III. REFLECTION AND TRANSMISSION FROM N PRINTED LAYERS

In this section, we summarize the EM response of an arbitrary number N of stacked dielectric layers, each printed with the same transverse orthogonal lattice of metallization. For convenience, the multilayer response is first presented in general, in terms of the shunt susceptance of the basic metallization, and then the shunt susceptance for a particular metallization will be described.

A. Stacked Metallized Multilayer in the Waveguide Aperture

According to the previous section, the expressions providing the reflection and transmission coefficients for the multilayer inserted inside the waveguide are those derived for oblique plane-wave incidence if we make the following substitution:

$$\cos(\theta)\,(\text{plane-wave incidence}) \;\leftrightarrow\; \cos(\theta_{nm}) = \frac{\beta_{nm}}{k_0}. \tag{9}$$

Further, TE/TM plane-wave incidence corresponds to $\mathrm{TE}_{nm}/\mathrm{TM}_{nm}$ guide mode excitations. The reflection and transmission can be written in compact form for either excitation by introducing the index $i \in \{1, -1\} \equiv \{\mathrm{TE}_{nm}, \mathrm{TM}_{nm}\}$. For the reflection coefficient off the N-layer multilayer of Fig. 2, we have [16]–[18] (10) and (11),[1] shown at the bottom of this page, where

$$\begin{aligned}
\Psi^{(i)} &\equiv j\sin\left(k_0 cn\cos\theta_{nm}^{d}\right) + \cos\left(k_0 cn\cos\theta_{nm}^{d}\right)\left(Y^{(i)}/2\right)\\
\tau^{(i)} &\equiv \cos\left(k_0 cn\cos\theta_{nm}^{d}\right) + \sin\left(k_0 cn\cos\theta_{nm}^{d}\right)\left(jY^{(i)}/2\right)\\
\zeta^{(i)} &\equiv \frac{\Psi^{(i)}}{\tau^{(i)}}\sqrt{1-\left(\frac{Y^{(i)}}{2\Psi^{(i)}}\right)^2}\\
\xi^{(i)} &= \frac{1-\zeta^{(i)}}{1+\zeta^{(i)}}.
\end{aligned} \tag{12}$$

In the above, the relative wave impedances for TE or TM modes in the regions $\alpha \in \{\text{air, dielectric}\} = \{a, d\}$ are

$$\eta_\alpha^{(i)} \equiv \frac{\eta_\alpha}{\cos^i\,\theta_{nm}^{\alpha}}, \qquad i \in \{1, -1\} \tag{13}$$

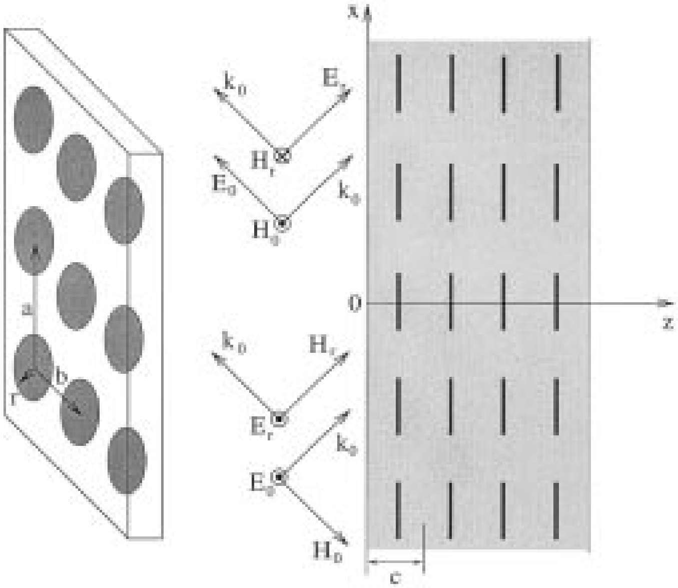

Fig. 2. Plane-wave incidence on PBG material made of PEC disks embedded in a dielectric host. The incidence angle equals the waveguide angle θ_{nm}.

where, for nonmagnetic host

$$\eta_\alpha \equiv \sqrt{\frac{\mu_\alpha}{\epsilon_\alpha}} = \frac{1}{n_\alpha} \tag{14}$$

and the mode angle inside the dielectric is given by Snell's law

$$\cos\theta_{nm}^{d} = \sqrt{1-\frac{\sin\theta_{nm}^{2}}{n_d^2}} = \sqrt{1-\frac{k_{nm}^2}{k_0^2 n_d^2}}. \tag{15}$$

Further, Y is the surface susceptance of the 2-D planar array of scatterers embedded within the host dielectric.

B. Shunt Susceptance of a Planar Periodic Metallization

The final ingredient to be supplied for the filter response is the calculation for the shunt susceptance of a *single* planar lat-

$$\Gamma_N^{(i)}(nm) = \frac{\dfrac{1-\left(\xi^{(i)}\right)^N}{2\sqrt{1-\left(\dfrac{Y^{(i)}}{2\Psi^{(i)}}\right)^2}}\left[\left(\dfrac{\eta_d^{(i)}}{\eta_a^{(i)}}-\dfrac{\eta_a^{(i)}}{\eta_d^{(i)}}\right)-\left(\dfrac{\eta_a^{(i)}}{\eta_d^{(i)}}+\dfrac{\eta_d^{(i)}}{\eta_a^{(i)}}\right)\dfrac{Y^{(i)}}{2\Psi^{(i)}}\right]}{1+\left(\xi^{(i)}\right)^N+\dfrac{1-\left(\xi^{(i)}\right)^N}{2\sqrt{1-\left(\dfrac{Y^{(i)}}{2\Psi^{(i)}}\right)^2}}\left[\left(\dfrac{\eta_d^{(i)}}{\eta_a^{(i)}}+\dfrac{\eta_a^{(i)}}{\eta_d^{(i)}}\right)+\left(\dfrac{\eta_a^{(i)}}{\eta_d^{(i)}}-\dfrac{\eta_d^{(i)}}{\eta_a^{(i)}}\right)\dfrac{Y^{(i)}}{2\Psi^{(i)}}\right]} \tag{10}$$

$$T_N^{(i)}(nm) = \frac{2}{\left[\left(1+\zeta^{(i)}\right)\tau^{(i)}\right]^N} \times \left\{1+\left(\xi^{(i)}\right)^N+\frac{1-\left(\xi^{(i)}\right)^N}{2\sqrt{1-\left(\dfrac{Y^{(i)}}{2\Psi^{(i)}}\right)^2}}\left[\left(\frac{\eta_d^{(i)}}{\eta_a^{(i)}}+\frac{\eta_a^{(i)}}{\eta_d^{(i)}}\right)+\left(\frac{\eta_a^{(i)}}{\eta_d^{(i)}}-\frac{\eta_d^{(i)}}{\eta_a^{(i)}}\right)\frac{Y^{(i)}}{2\Psi^{(i)}}\right]\right\}^{-1} \tag{11}$$

---

[1] These formulas are generalizations of the ones for normal incidence derived in [18]

tice of printed metallic elements, immersed in the host dielectric. In this paper, we will consider printed disks of fairly large diameter.

For a general TE plane-wave incidence, corresponding through (9) to a TE_{nm} waveguide mode, and denoted by the excitation field $\mathbf{E}_0$, we can follow the approach of [19] and write the effect of this array as a shunt susceptance $Y = jB$ that is connected with the reflection coefficient of the corresponding standing-wave mode by

$$R = \frac{-jB}{2}. \tag{16}$$

The normal modes of the single planar array are found by solving Maxwell's equations for 2-D unit cell composed of two perfect electric conductor (PEC) [perfect magnetic conductor (PMC)] walls along the boundaries perpendicular to the **E** (**H**)-field, for TE (TM) polarization, along with two periodic boundary conditions (PBCs) walls perpendicular to the above, satisfying Floquet's theorem. This is a waveguiding structure problem pertaining to the symmetries of the transverse unit cell under plane-wave incidence, and the resulting modes should not be confused with those of the actual rectangular waveguide.

Applying the reciprocity theorem, we find for the reflected field

$$\mathbf{E}_r = b_0 \hat{\mathbf{y}} e^{jk(\cos\theta^d_{nm} z - \sin\theta^d_{nm} x)} \tag{17}$$

the result

$$\begin{aligned} b_0 ab(\eta_d)^{-1}\cos\theta^d_{nm} &= -\int_0^{2\pi}\int_0^r \hat{\mathbf{y}} e^{jk\sin\theta^d_{nm} x}\cdot\mathbf{J}\rho\, d\rho\, d\phi \\ &\equiv -I \end{aligned} \tag{18}$$

where $k \equiv nk_0$ and $\mathbf{J}$ is the total impressed current density on the illuminated side S of the disk, which is, in general, a function of the excitation, i.e., $\mathbf{J} = \mathbf{J}(\mathbf{E}_0)$. The shunt susceptance B is given as

$$B = \frac{jI\eta_d}{abE_0\cos\theta^d_{nm}} \tag{19}$$

where it is understood that only real terms on the right-hand side of (19) (imaginary terms in the current I) will be included in B.

To compute the reflection coefficient, some solution to the scattering problem that provides the current **J** *must* be provided. In this paper, we will use an analytical expression for the disk current [20] of the form

$$\begin{aligned} \mathbf{J} = \frac{4r^2}{\pi}\frac{\dfrac{E_0}{\eta_d}}{\sqrt{1-\left(\dfrac{\rho}{r}\right)^2}} &\left[\hat{\mathbf{x}}\sum_{q,s=0}^{\infty}\chi_{qs}(kr,\theta^d_{nm})\sin^s\phi\cos^q\phi\right. \\ &\left. +\hat{\mathbf{y}}\sum_{q,s=0}^{\infty}\psi_{qs}(kr,\theta^d_{nm})\sin^q\phi\cos^s\phi\right] \end{aligned} \tag{20}$$

where the functions $\chi_{qs}(kr,\theta^d_{nm})$, $\psi_{qs}(kr,\theta^d_{nm})$ are dimensionless perturbative expansions of kr, obtained from successive derivatives of the incident field on a single disk inside a transverse unit cell. Expressions for these derivative expansions can be found in [20].

Substituting (20) into (18) and Taylor expanding the exponential, we obtain

$$\begin{aligned} I = \frac{2r^2}{\pi}\frac{E_0}{\eta_d}\sum_{l=0}\frac{j^l\sin^l\theta^d_{nm}}{l!}&\sum_{q,s=0}(kr)^l\psi_{qs}(kr,\theta^d_{nm}) \\ \cdot B\left(\frac{l+q+s}{2}+1,\frac{1}{2}\right)&\int_0^{2\pi}\sin^q\phi\cos^{s+l}\phi\, d\phi \end{aligned} \tag{21}$$

where $B(u,v)$ is the Euler Beta function. This expression provides the shunt susceptance as a perturbative expansion in electrical disk size kr to a degree of accuracy commensurate with the order (in kr) up to which the functions $\chi_{qs}(kr,\theta^d_{nm})$, $\psi_{qs}(kr,\theta^d_{nm})$ have been calculated. We note here that a given power in kr for the final current integral (21) does not uniquely correspond to a specific multipole order. Due to the series product in (21), the maximum power in kr to which this integral is truncated involves mixing of lower order multipoles and higher order multipoles, which we will demonstrate below. In our opinion, the expansion of (21) should be considered as asymptotic, rather than convergent.

In this paper, we will include the leading order (LO) and next-to-leading order (NLO) for the current integral. We have calculated the following necessary functions, up to $\mathcal{O}((kr)^3)$, using Eggimann's formulas:

$$\begin{aligned} \psi_{00} = &\frac{kr}{315}j\left\{210(2-\sin^2\theta^d_{nm})+(kr)^2\right. \\ &\left.\cdot[196-56\sin^2\theta^d_{nm}+7\sin^4\theta^d_{nm}]\right\} \end{aligned} \tag{22}$$

$$\begin{aligned} \psi_{10} =&0 \\ \psi_{01} =&\frac{1}{30}\sin\theta^d_{nm}\left\{-30+(kr)^2\left[22-13\sin^2\theta^d_{nm}\right]\right\} \\ &-\frac{4}{9\pi}j(kr)^3\sin\theta^d_{nm} \end{aligned} \tag{23}$$

$$\begin{aligned} \psi_{20} =&\frac{kr}{315}j\left\{-210(2-\sin^2\theta^d_{nm})+(kr)^2\right. \\ &\left.\cdot\left[-224+73\sin^2\theta^d_{nm}-11\sin^4\theta^d_{nm}\right]\right\} \\ \psi_{11} =&0 \\ \psi_{02} =&\frac{kr}{315}j\left\{-210(1-2\sin^2\theta^d_{nm})-(kr)^2\right. \\ &\left.\cdot\left[56+38\sin^2\theta^d_{nm}-46\sin^4\theta^d_{nm}\right]\right\} \end{aligned} \tag{24}$$

$$\begin{aligned} \psi_{30} =&0 \\ \psi_{21} =&-\frac{7}{30}(kr)^2\sin\theta^d_{nm}(3-\sin^2\theta^d_{nm}) \\ \psi_{12} =&0 \\ \psi_{03} =&\frac{1}{30}(kr)^2\sin\theta^d_{nm}(-13+22\sin^2\theta^d_{nm}) \end{aligned} \tag{25}$$

$$\begin{aligned} \psi_{40} =&\frac{1}{315}(kr)^3j\left\{28-17\sin^2\theta^d_{nm}+4\sin^4\theta^d_{nm}\right\} \\ \psi_{31} =&0 \\ \psi_{22} =&\frac{1}{315}(kr)^3j\left\{35+53\sin^2\theta^d_{nm}-52\sin^4\theta^d_{nm}\right\} \\ \psi_{13} =&0 \\ \psi_{04} =&\frac{1}{315}(kr)^3j\left\{7+46\sin^2\theta^d_{nm}-80\sin^4\theta^d_{nm}\right\}. \end{aligned} \tag{26}$$

Keeping terms in the Taylor expansion of the exponential (multipole expansion) consistently up to $l=3$, we have

$$I(l=0)=\frac{E_0}{\eta_d}\,\frac{16}{3}\,r^2(kr)j\left\{1+(kr)^2\left[\frac{8}{15}-\frac{1}{6}\,\sin^2\theta_{nm}^d\right]\right\}. \tag{27}$$

The rest of the terms, to be included for consistency at this order, are

$$\begin{aligned}I(l=1)={}&\frac{E_0}{\eta_d}\,\frac{8}{3}\,r^2(kr)j\sin^2\\&\cdot\theta_{nm}^d\left\{-1+\frac{(kr)^2}{3}\left[1+\frac{4}{25}\,\sin^2\theta_{nm}^d\right]\right\}\end{aligned} \tag{28}$$

$$I(l=2)=-\frac{E_0}{\eta_d}\,\frac{8}{45}\,r^2(kr)^3\sin^2\theta_{nm}^d\left[5+2\sin^2\theta_{nm}^d\right] \tag{29}$$

and

$$I(l=3)=\frac{E_0}{\eta_d}\,\frac{8}{45}\,r^2(kr)^3j\sin^4\theta_{nm}^d. \tag{30}$$

From (18), we obtain the shunt susceptance as

$$\begin{aligned}B={}&\frac{16}{3}\,\frac{r}{b}\,\frac{r}{a}\,\frac{kr}{\cos\theta_{nm}^d}\left\{1-\frac{\sin^2\,\theta_{nm}^d}{2}+(kr)^2\right.\\&\left.\cdot\left[\frac{8}{15}-\frac{\sin^2\,\theta_{nm}^d}{6}-\frac{\sin^4\,\theta_{nm}^d}{150}\right]\right\}.\end{aligned} \tag{31}$$

We can separate the above expression in two parts. The two terms of the LO contribution

$$B_{\mathrm{LO}}=\frac{16}{3}\,\frac{r}{b}\,\frac{r}{a}\,\frac{kr}{\cos\theta_{nm}^d}\left\{1-\frac{\sin^2\theta_{nm}^d}{2}\right\} \tag{32}$$

correspond respectively to the point-like electric and magnetic dipole contributions. If increased accuracy is desired, the lattice interaction constants for the point dipole (PD) contributions may be included, and this is what we will implement in this paper. We, therefore, perform the substitution

$$\begin{aligned}B_{\mathrm{LO}}\to B_{\mathrm{PD}}={}&\frac{16}{3}\,\frac{r}{b}\,\frac{r}{a}\,\frac{kr}{\cos\theta_{nm}^d}\\&\cdot\left[\frac{1}{1-\frac{8}{3}\left(\frac{r}{a}\right)^3C_e}-\frac{\sin^2\theta_{nm}^d}{2}\right.\\&\left.\cdot\frac{1}{1-\frac{4}{3}\left(\frac{r}{a}\right)^3C_m}\right]\end{aligned} \tag{33}$$

where C_e, C_m are the lattice interaction constants, accounting for the interactions of the electric and magnetic PDs in the transverse infinite lattice. These interaction constants have been calculated in [21] and are summarized in the Appendix. The final expression giving the total shunt susceptance, including NLO contributions, is a combination of (33) and (31) as follows:

$$\begin{aligned}B={}&B_{\mathrm{PD}}+\frac{16}{3}\,\frac{r}{b}\,\frac{r}{a}\,\frac{kr}{\cos\theta_{nm}^d}(kr)^2\left[\frac{8}{15}-\frac{\sin^2\,\theta_{nm}^d}{6}\right.\\&\left.-\frac{\sin^4\,\theta_{nm}^d}{150}\right].\end{aligned} \tag{34}$$

It will be noticed that (34) contains lattice interaction constants for the point-like dipole part of the disk current, while the higher order corrections are directly included from the disk current and do not further recognize existence of the lattice. To the best of our knowledge, lattice interactions for higher multipoles or for the frequency-dependent form factors of the dipoles themselves have never been calculated, nor is it clear that they can be meaningfully defined. We anticipate that our formulas can be very accurate for medium disk sizes, but will start braking down as the printed implants start touching each other. Ultimately, the range of validity of the above formulas depends on the accuracy required and, for implants of significant size, should be compared to numerical methods. Full-wave codes, however, have their own convergence and accuracy limitations, in addition to being very CPU time consuming. Experiments are certainly the most direct approach for validating both our method and the design possibilities it offers. In the following section, we turn to a double comparison of our theory with both experiments and full-wave HFSS simulations.

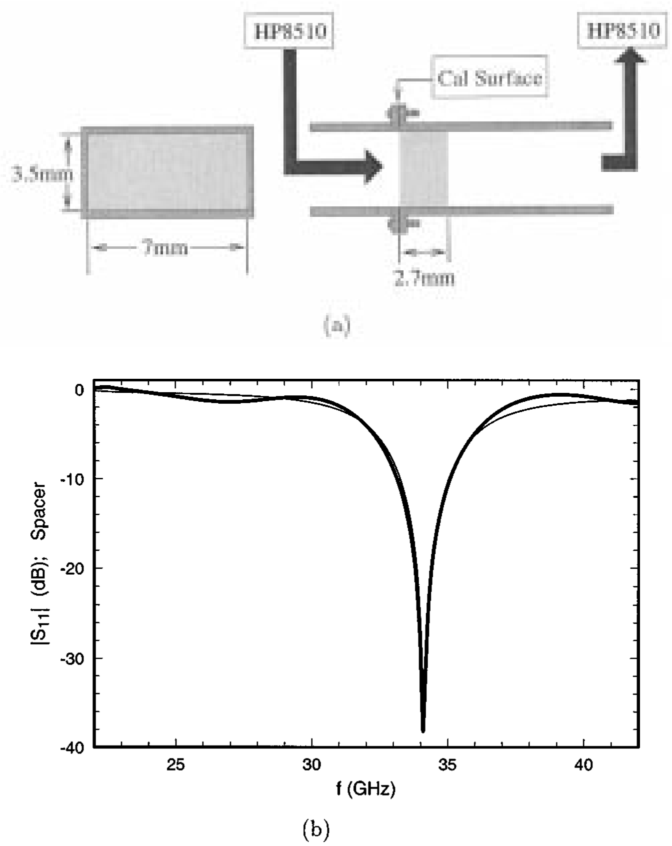

Fig. 3. (a) Setup for permittivity measurement of host dielectric. (b) Theoretical (thin solid) and experimental (heavy solid) plots of the reflected power.

In this paper, we will examine the filtering behavior of the printed layers for the dominant waveguide mode only TE_{10}.

C. Fabrication and Measurements

We have selected a Ka-band waveguide to perform the experiments, with standard dimensions $a_w=2b_w=0.7$ cm. The corresponding dominant-mode frequency band for the TE_{10} mode is

$$f\in\left\{\frac{15}{a_w(\mathrm{cm})},\,\frac{30}{a_w(\mathrm{cm})}\right\}\ \mathrm{GHz}=\{21.428,\,42.857\}\ \mathrm{GHz}. \tag{35}$$

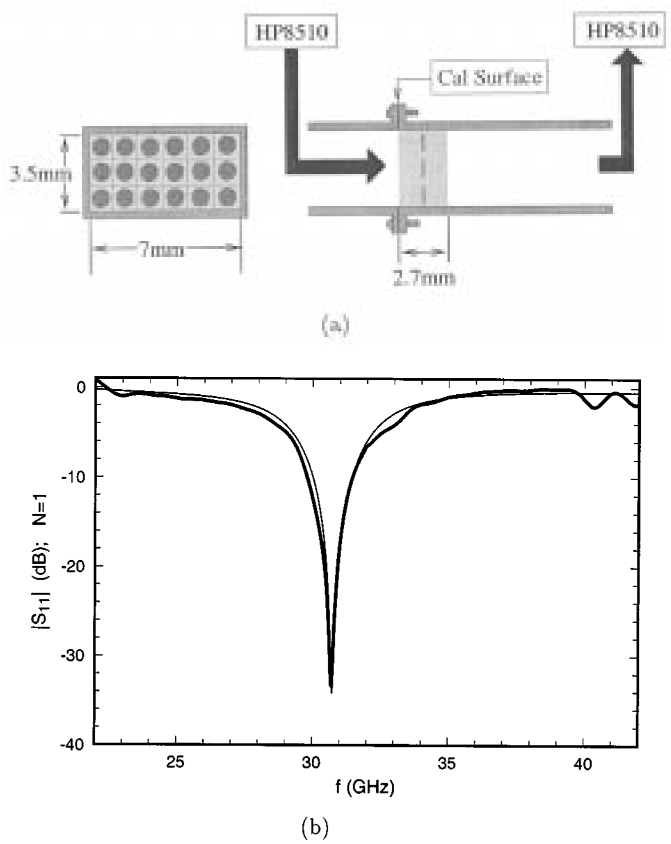

(a)

(b)

Fig. 4. (a) Measurement of one printed PBG layer inserted in the waveguide. (b) Theoretical (thin solid) and experimental (heavy solid) plots of the reflected power.

For the layer thickness, we have selected $c = 0.268$ cm, which provides a longitudinal PBG in the second half of the main-mode band. This design is not sufficiently fine tuned to guarantee optimum filtering characteristics of the system, but it intends to validate the theory and, at the same time, present all the details of the EM propagation of the main mode through the filter.

The measurements were calibrated by a "response" calibration procedure, where each empty piece of waveguide was considered in conjunction with the calibration standards. This way, the reflection coefficients up to the filter interface are directly measured. For increased accuracy, we have divided the frequency range into two independently calibrated ranges, meeting at 32 GHz. Further, we have gated the results during calibration, and further fine tuned the gating during measurements of the structures, using as a guideline the smooth joining of the responses at 32 GHz. This latter amount of gating was, in all cases, either very minimal or unnecessary.

We first performed an experiment to accurately measure the dielectric constant of the substrate at the frequency range of (35) and for the actual temperature/humidity conditions of the experiment. Setting in the formulas $r = 0$, we obtain an exact solution for a homogeneous dielectric slab inserted in the waveguide of thickness Nc. For $N = 1$, one Fabry–Perot resonance is expected in the waveguide. Each layer has a measured thickness $c = 2.68$ mm, and the permittivity of the duroid we used was rated by the manufacturer as $\epsilon_d = 10.8(1 - j0.0028)$. In Fig. 3, we fit the experimental resonance perfectly if we choose the dielectric permittivity to be $\epsilon_d = 11.1(1 - j0.0028)$, which is at the edge of the uncertainty value suggested by the manufacturer. We will use this measured permittivity value, for all subsequent comparisons with experiments. Strictly speaking, the position of the resonance in Fig. 3 fixes the product $\sqrt{\epsilon_d}c$, but since the thickness c has been measured at two significant digits (in millimeters), any additional uncertainty in c should be thought of as absorbed in the determination of ϵ_d.

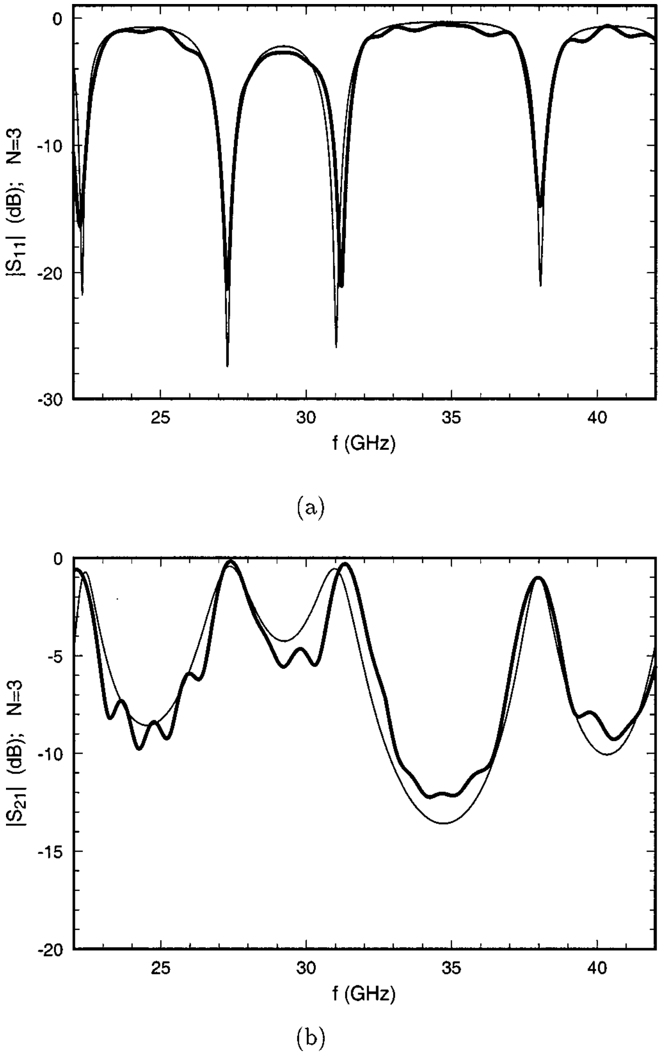

(a)

(b)

Fig. 5. (a) Comparison between theoretical (thin solid) and experimental (heavy solid) reflection for $N = 3$. (b) Same for transmission.

The basic building block of the filter is shown in Fig. 4. The metallization is embedded within the host dielectric layer, but in our experiment, we used two half-thickness layers to recreate this section: one metallized and one completely etched. Further, for all the experiments reported in this paper, layers were stacked and press fit at the end of one waveguide section, with no adhesive in between. The transverse unit cell has been chosen square and a 3×6 lattice of disks was actually printed with aspect ratios $r/a = 0.34$ and $a/c = 0.68$, as shown in Fig. 4. The aspect ratio $r/a = 0.34$ was measured after etching, thus, over etching has been accounted for (the mask was designed with $r/a = 0.4$). We see that the measurements are in excellent

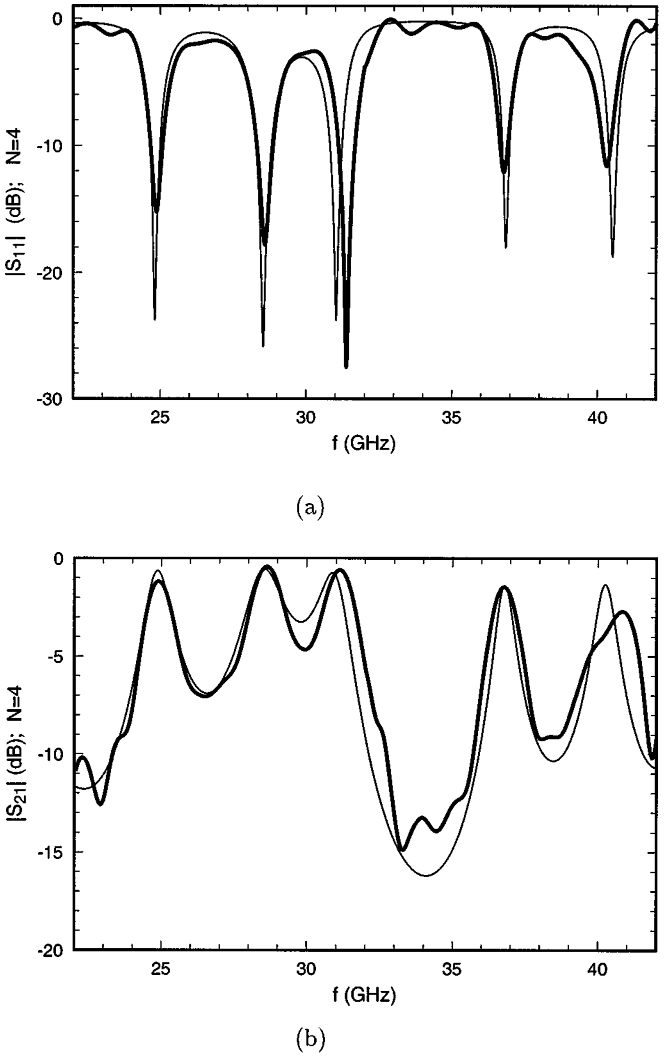

Fig. 6. (a) Comparison between theoretical (thin solid) and experimental (heavy solid) reflection for $N = 4$. (b) Same for transmission.

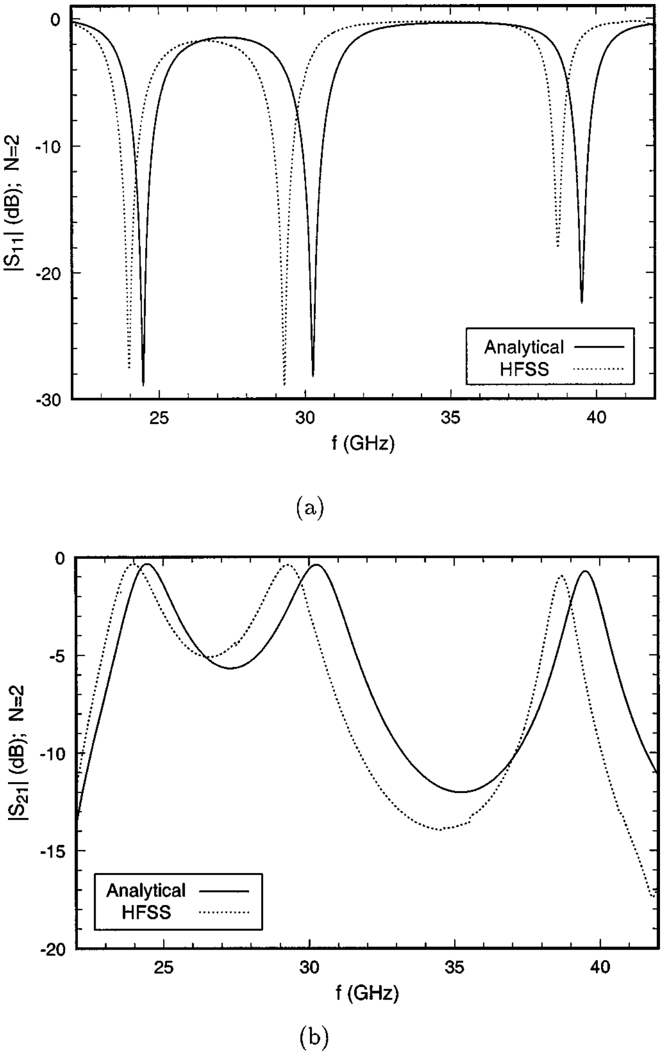

Fig. 7. (a) Comparison between analytical (solid) and HFSS (dotted) reflection for $N = 2$. (b) Same for transmission.

agreement with our theory, and the resonance has been significantly shifted as a result of the scattering off the single lattice of printed elements.

In Fig. 5, we show measurements and theoretical results for $N = 3$, at excellent agreement to each other. The PBG is clearly visible around 34 GHz, with 13-dB isolation, among distorted Fabry–Perot resonances.

In Fig. 6, we show experimental and analytical results for $N = 4$, again in very good agreement to each other. While the number of Fabry–Perot oscillations increases with increasing N, the band gap remains fixed in frequency, and is by design a property of the PBG material, not of the number of sections.

D. Optimized Passband Filters

After validating our theory by comparison to measured data in the previous section, we now turn to the design of extremely flat short passband waveguide filters using the printed PBG layers. The physics of these layers is clear: for a fixed frequency window, such as the one that corresponds to our Ka-band waveguide, high-frequency isolation is produced by the bandgap, which is deeper for increasing printed element size and thinner printed layers. Positioning of the bandgap is due mainly to the layer electrical thickness kc, with the end of the first bandgap at $n^r k_0 c \,\mathrm{Re}\{\cos\theta^d_{nm}\} = \pi$. Flatness of the passband depends on the element size kr or, alternatively r/a and the number of actual printed elements within the waveguide mouth. It turns out that the printed layers have superb filtering properties for fairly large disks, as we will report in this section. We have not fabricated the optimized filters in this section, but our theory was validated by the previous measurements. Further, we compare our analytical predictions with HFSS simulations of the same structure.

For the HFSS simulations, we have subdivided the printed disks into 20-sided regular polygons, and the frequency domain into frequency subdomains each containing a single reflection resonance. It turns out that this allows us the maximum numerical stability within our machine's memory limits. Each simulation over a limited frequency range of 5 GHz has taken approximately 12 h (real time), a total of two days per plot.

In Fig. 7, we show the comparison for two printed layers of the nonoptimized design. We see that the response is the same

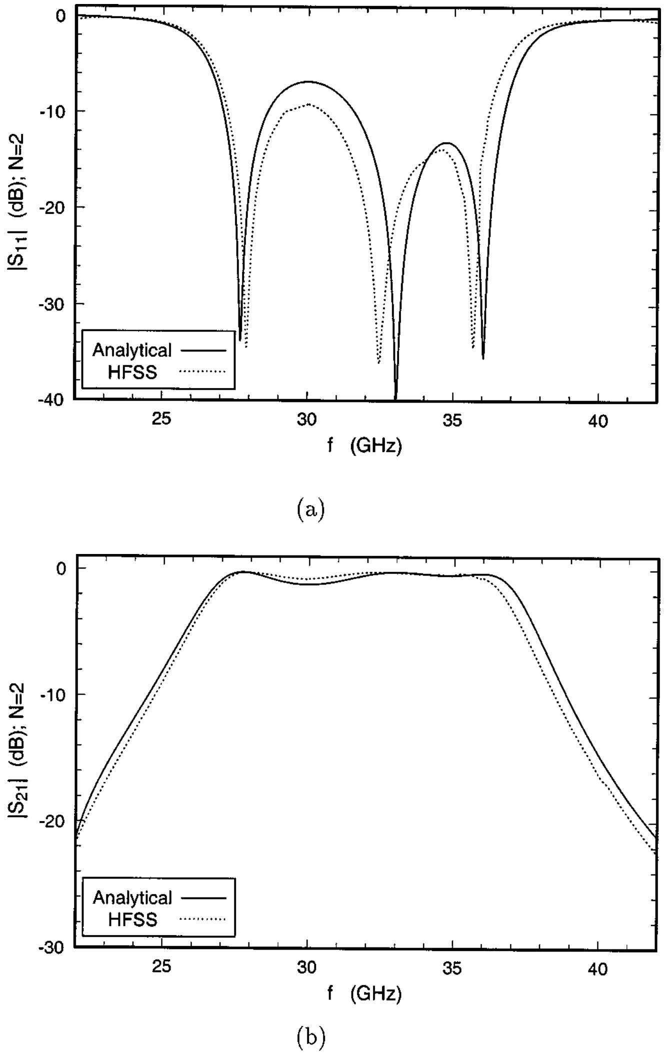

Fig. 8. (a) Comparison between analytical (solid) and HFSS (dotted) reflection for $N = 2$. (b) Same for transmission.

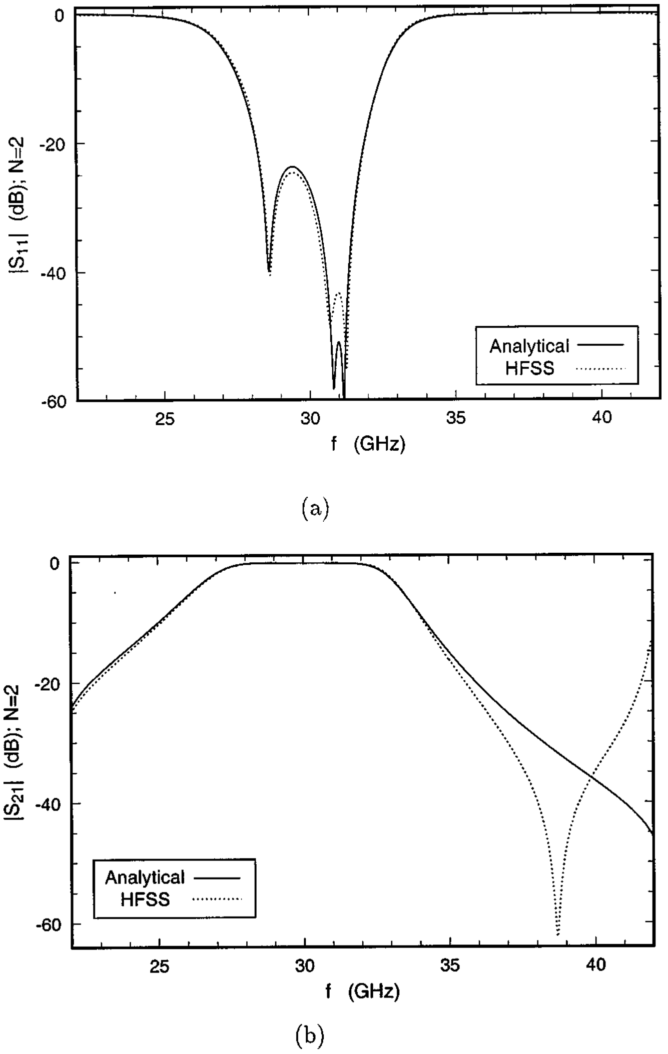

Fig. 9. (a) Comparison between analytical (solid) and HFSS (dotted) reflection for $N = 2$. (b) Same for transmission.

for both analytical and HFSS predictions, but the HFSS has, for this design, a shift in the resonances of 2%–3%. Given that this design was also measured with excellent agreement to our analytical calculation, we conclude that HFSS shows some inaccuracy in positioning the resonances *for the specific electrical sizes involved*. This may be due to the small size of printed elements, which imposes an increased number of divisions in the finite-element mesh, thus increasing the problem size and ultimately affecting the result accuracy.

In Fig. 8, we increase the interaction between adjacent printed layers by using a shorter thickness $c = 1.7$ mm in a 3×6 transverse printed lattice of larger disks $r/a = 0.45$. We are using $N = 2$ and observe the beginning of the formation of a flat passband. The bandgap on the right of the figure is deeper and larger, "pushing" the Fabry–Perot reflection resonances close together. We further see that, for these larger printed elements, the agreement between our theory and HFSS is markedly better.

In Fig. 9, we show an optimized design with $c = 1.7$ mm, $r/a = 0.45$, and a transverse lattice of 2×4 disks, which are, therefore, much larger. We see that agreement between our theory and HFSS is excellent, except for the early reflection resonance at the high edge of the band. The disagreement may be due to the truncation of our perturbative method to finite-order multipoles. Further, since the disks are almost touching, the mesh employed by HFSS may not capture the region between adjacent disks in sufficient detail. At any rate, the disagreement is below the -30-dB level and does not affect our conclusions. We have used only two printed layers, but the resulting structure is an excellent filter with deep isolation and very flat passband.

In Fig. 10, we present the passband of the last design in detail, which shows a completely flat response, of only 0.25-dB insertion loss. The total length of the filter is $1.7 \times N$ mm, which, for $N = 2$, is a tiny size (slightly smaller than the narrow guide dimension) given its performance. Obviously, the main advantage of the filter performance is the flat passband and the deep isolation created with a very small number of layers. Electrically, each layer is still a dielectric half-wavelength, but the performance characteristics are due to the completely distributed and highly symmetric nature of the scatterers.

Notice further the transition from Fig. 8 to that of the optimum filter of Fig. 9 is realized without increasing the length of the

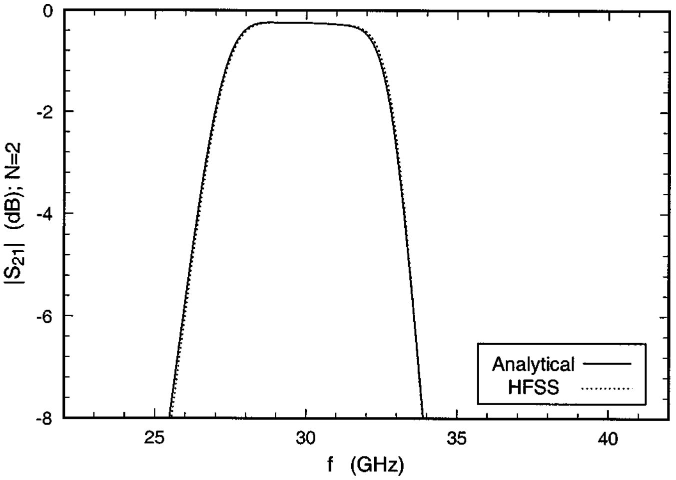

Fig. 10. Flat passband of optimized filter for two layers: Analytical (solid) and HFSS (dotted).

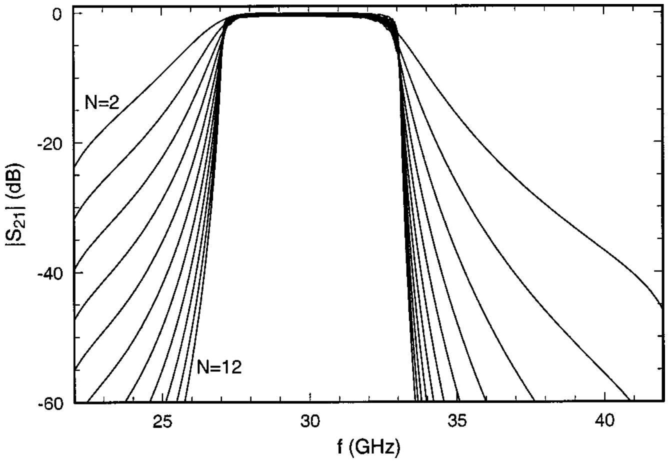

Fig. 11. Passband filter characteristics as a function of printed layer number N.

filter, but by simply increasing the electrical size of the printed elements, a design option that is of no extra cost.

In Fig. 11, we present the filtering characteristics of the previous design, as a function of sections N. We see that the isolation and slope increase very fast while the passband is maintained virtually without ripples. It is important to know that the filter response is not periodic. As the frequency increases (e.g., from 40 to 80 GHz), the printed layers behave increasingly as lossy conductors and no further passbands are visible. This tendency is evident in the quadratic increase in frequency of the shunt susceptance (34) and signifies that the PBG material evolves from a dielectric to a metallic phase.

An important application is the issue of designing narrow-band waveguide filters, using the shortest and most inexpensive structures possible. Using our printed PBG layers, we can essentially narrow the passband by increasing the size r/a (to almost touching disks).

IV. CONCLUSION

We have developed a new class of filters that are compact and of adjustable thickness (modular). They are multilayered structures stacked along the propagating direction of the waveguide monolithically without air separation. Each layer consists of a 2-D planar array of metallic elements printed on a low-loss dielectric substrate. Reflection on the waveguide walls creates a laterally infinite lattice, equivalent to a 2-D photonic crystal. This planar periodicity and the PBG properties enhance the frequency selectivity of each layer, thus creating a length reduction compared to existing devices, while maintaining a low ripple level. Production cost is maintained at low levels by applying traditional photolithographic array printing.

We have presented a theoretical analysis of the filter response based on the response of the corresponding laterally infinite three-dimensional crystal to a TE or TM plane-wave excitation. We have employed diffraction theory of circular disks to expand the analysis from the low-frequency limit for increasing size of the metallic elements. Our approach has been validated by experiments in the Ka-band and been proven to be in good agreement with numerical results obtained through HFSS. In this sense, the theoretical method provides an extremely accurate tool for the analysis and synthesis of this type of filters with a huge computational advantage (1000 points/s). Moreover, our approach may be readily generalized to any shape of metallization other than the circular disk.

The range of potential of the structure covers frequency selectivity in a single-plexing or multiplexing manner, as well as harmonic extraction. It has been pointed out that the bandgap location scales as $n^r k_0 c \,\mathrm{Re}\{\cos\theta^d_{nm}\} = \pi$ and differs for each waveguide harmonic since each mode corresponds to different $\cos\theta^d_{nm}$. At a particular frequency where two or more modes propagate, it is possible to position the corresponding bandgaps by an appropriate selection of the crystal geometry and constitution. In this manner, one of the harmonics is extracted to propagate while the others face a stopband. Furthermore, the proposed structure performs independently of waveguide shape and is scalable to any waveguide size and waveguide mode.

APPENDIX

The electric and magnetic point–dipole lattice interaction constants have been calculated in [21]. The normalized electric dipole constant is

$$\begin{aligned} C_e = {} & \frac{1.2}{\pi}\left(\frac{a}{b}\right)^3 + \frac{(ka)^2}{2\pi} \\ & \cdot \left[-\frac{a}{b}\ln\left(\frac{4\pi b}{a}\right) + \frac{a}{2b} + \frac{(ka)(kb)}{48} \right. \\ & + j\left(\frac{ka}{3} - \frac{\pi}{kb\cos\theta^d_{nm}}\right) \\ & \left. + \frac{a}{b}\pi \sum_{l=1}^{\infty}\left(\frac{1}{a\Gamma_l} + \frac{1}{a\Gamma_{-l}} - \frac{1}{l\pi}\right)\right] \\ & - \frac{2}{\pi}\frac{a}{b}\sum_{l=1}^{\infty}\sum_{p=1}^{\infty}(\gamma_l a)^2 \cos(pka\sin\theta^d_{nm}) K_0(p\gamma_l a) \end{aligned} \quad (36)$$

where K_0 is the modified Bessel function of the second kind, and the propagation constants for the free-standing 2-D printed implant lattice are

$$\Gamma_l = \sqrt{\left(\frac{2l\pi}{a} + k\sin\theta_{nm}^d\right)^2 - k^2} \quad \gamma_l = \sqrt{\left(\frac{2l\pi}{b}\right)^2 - k^2}. \tag{37}$$

Similarly, the normalized magnetic dipole lattice constant is

$$\begin{aligned} C_m = & -\frac{1}{2\pi}\left[1.2\left(\frac{a}{b}\right)^3 + \frac{\pi^2}{3}\frac{a}{b}\right] - \frac{(ka)^2}{4\pi} \\ & \cdot \left[\frac{a}{b}(1-\gamma) + \frac{a}{b}(1-\cos kb)\ln\left(\frac{8\pi}{(ka)(kb)}\right)\right. \\ & + \frac{(ka)(kb)}{48} - 2j\left(\frac{ka}{3} - \frac{\pi\sin^2\theta_{nm}^d}{kb\cos\theta_{nm}^d}\right) \\ & - 2\frac{a}{b}\pi\sum_{l=1}^{\infty}\left(\frac{1}{a\Gamma_l} + \frac{1}{a\Gamma_{-l}} - \frac{1}{l\pi}\right) \\ & \left. -2\frac{a}{b}\pi\sum_{l=1}^{\infty}\left(\frac{a\Gamma_l + a\Gamma_{-l}}{(ka)^2} + \frac{1}{2l\pi} - \frac{4l\pi}{(ka)^2}\right)\right] \\ & + \frac{2}{\pi}\frac{a}{b}\sum_{l=1}^{\infty}\sum_{p=1}^{\infty}(\gamma_l a)^2\cos(pka\sin\theta_{nm}^d) \\ & \cdot\left(K_0(p\gamma_l a) - \frac{\gamma_l a}{p}K_1(p\gamma_l a)\right) \end{aligned} \tag{38}$$

where γ is Euler's constant.

Concentrating on a square lattice $a = b$, we can first use a Taylor expansion for the Bessel functions

$$\begin{aligned} & K_0(p\gamma_l a) \\ & \quad = K_0(2\pi lp) + \pi lp\left(\frac{ka}{2\pi l}\right)^2 K_1(2\pi lp) \end{aligned} \tag{39}$$

$$\begin{aligned} & K_1(p\gamma_l a) \\ & \quad = K_1(2\pi lp) - \left(\frac{ka}{2\pi l}\right)^2\left[\frac{1}{2}K_1(2\pi lp) - \pi lpK_2(2\pi lp)\right] \end{aligned} \tag{40}$$

where we have used the formula

$$\left(\frac{1}{z}\frac{d}{dz}\right)^k\left\{z^{-\nu}e^{-j\nu\pi}K_\nu(z)\right\} = z^{-\nu-k}e^{-j(\nu+k)\pi}K_{\nu+k}(z). \tag{41}$$

Further, the double sums in (36) and (38) can be approximated by their leading term $l = p = 1$ only since the Bessel functions K_0, K_1, and K_2 are extremely suppressed for larger arguments. The final result is

$$\begin{aligned} C_e = & \frac{1}{\pi}\left[1.2 - 8\pi^2 K_0(2\pi)\right] + \frac{(ka)^2}{2\pi} \\ & \cdot\left[-\ln 4\pi + \frac{1}{2} + \frac{(ka)^2}{48} + j\left(\frac{ka}{3} - \frac{\pi}{ka\cos\theta_{nm}^d}\right)\right. \\ & \left. +\pi\sum_{l=1}^{\infty}\left(\frac{1}{a\Gamma_l} + \frac{1}{a\Gamma_{-l}} - \frac{1}{l\pi}\right)\right] \\ & + (ka)^2\left[\left(\frac{2}{\pi} + 4\pi\sin^2\theta_{nm}^d\right)K_0(2\pi) - 2K_1(2\pi)\right] \end{aligned} \tag{42}$$

and

$$\begin{aligned} C_m = & -\frac{1}{2\pi}\left[1.2 + \frac{\pi^2}{3} - 8\pi K_1(2\pi)\right] - \frac{(ka)^2}{4\pi} \\ & \cdot\left[1 - \gamma + (1-\cos ka)\ln\left(\frac{8\pi}{(ka)^2}\right) + \frac{(ka)^2}{48}\right. \\ & - 2j\left(\frac{ka}{3} - \frac{\pi\sin^2\theta_{nm}^d}{ka\cos\theta_{nm}^d}\right) \\ & - 2\pi\sum_{l=1}^{\infty}\left(\frac{1}{a\Gamma_l} + \frac{1}{a\Gamma_{-l}} - \frac{1}{l\pi}\right) \\ & \left. -2\pi\sum_{l=1}^{\infty}\left(\frac{a\Gamma_l + a\Gamma_{-l}}{(ka)^2} + \frac{1}{1l\pi} - \frac{4l\pi}{(ka)^2}\right)\right] \\ & + \frac{(ka)^2}{\pi}\Big[2K_0(2\pi) - K_2(2\pi)\Big]. \end{aligned} \tag{43}$$

The above formulas are to be readily substituted in (34) with the numerical values

$$\begin{aligned} \gamma &= 0.577 \\ K_0(2\pi) &= 0.49019 \times e^{-2\pi} \\ K_1(2\pi) &= 0.52775 \times e^{-2\pi} \\ K_2(2\pi) &= 0.65773 \times e^{-2\pi}. \end{aligned} \tag{44}$$

REFERENCES

[1] G. Matthaei, L. Young, and E. M. T. Jones, *Microwave Filters, Impedance Matching Networks and Coupling Structures*. Norwood, MA: Artech House, 1980, ch. 3, 4, 6–9.

[2] S. Cohn and R. Levy, "A history of microwave filter research, design and development," *IEEE Trans. Microwave Theory Tech.*, vol. MTT-32, pp. 1055–1067, Sept. 1984.

[3] G. Matthaei, "An overview of some important contributions to microwave engineering," in *IEEE MTT-S Int. Microwave Symp. Dig.*, 1989, p. 745.

[4] M. Piloni, R. Ravanelli, and M. Guglielmi, "Resonant aperture filters in rectangular waveguide," in *IEEE MTT-S Int. Microwave Symp. Dig.*, 1999, p. 911.

[5] R. Levy, H.-W. Yao, and K. A. Zaki, "Transitional combline/evanescent mode microwave filters," in *IEEE MTT-S Int. Microwave Symp. Dig.*, 1996, p. 461.

[6] R. V. Snyder, "Inverted resonator evanescent mode filters," in *IEEE MTT-S Int. Microwave Symp. Dig.*, 1996, p. 465.

[7] H.-W. Yao, K. A. Zaki, A. A. Atia, and R. Hershitg, "Full-wave modeling of conducting posts in rectangular waveguides and its application to slot coupled combline filters," *IEEE Trans. Microwave Theory Tech.*, vol. 43, pp. 2824–2830, Dec. 1995.

[8] K.-L. Wu, R. R. Mansour, and H. Wang, "A full wave analysis of a conductor post insert reentrant coaxial resonator in rectangular waveguide combline filters," in *IEEE MTT-S Int. Microwave Symp. Dig.*, 1996, p. 1639.

[9] H.-W. Yao, C. Wang, and K. A. Zaki, "Analysis of quarter wavelength ceramic combline filters," in *IEEE MTT-S Int. Microwave Symp. Dig.*, 1996, p. 473.

[10] S.-W. Chen and K. A. Zaki, "Dielectric ring resonators loaded in waveguide and on substrate," *IEEE Trans. Microwave Theory Tech.*, vol. 39, pp. 2069–2076, Dec. 1991.

[11] W. Sun and C. A. Balanis, "MFIE analysis and design of ridged waveguides," *IEEE Trans. Microwave Theory Tech.*, vol. 41, pp. 1965–1971, Nov. 1993.

[12] H. Contopanagos, N. G. Alexópoulos, and E. Yablonovitch, "High-Q rectangular cavities and waveguide filters using periodic metalo-dielectric slabs," in *IEEE MTT-S Int. Microwave Symp. Dig.*, 1998, p. 1539.

[13] B. Lenoir, D. Baillargeat, S. Verdeyme, and P. Guillon, "Finite element method for rigorous design of microwave devices using photonic band gap structures," in *IEEE MTT-S Int. Microwave Symp. Dig.*, 1998, p. 1061.

[14] C. M. Soukoulis, Ed., "Photonic band gap materials," in *Applied Sciences*. ser. NATO ASI E. Norwell, MA: Kluewer, 1996, vol. 315.

[15] *J. Opt. Soc. Amer. B, Opt. Phys. (Special Issue)*, 1993.

[16] C. A. Kyriazidou, H. Contopanagos, W. M. Merrill, and N. G. Alexópoulos, "Artificial versus natural crystals: Effective wave impedance for printed photonic band gap materials," *IEEE Trans. Antennas Propagat.*, vol. 48, pp. 95–106, Jan. 2000.

[17] H. F. Contopanagos, C. A. Kyriazidou, W. M. Merrill, and N. G. Alexópoulos, "Effective response functions for photonic band gap materials," *J. Opt. Soc. Amer. A, Opt. Image Sci.*, vol. 16, pp. 1682–1699, July 1999.

[18] H. Contopanagos, N. G. Alexópoulos, and E. Yablonovitch, "High-Q radio frequency structures using one-dimensionally periodic metallic films," *IEEE Trans. Microwave Theory Tech.*, vol. 46, pp. 1310–1312, Sept. 1998.

[19] R. E. Collin, *Field Theory of Guided Waves*, 2nd ed. New York: IEEE Press, 1991, pp. 764–772.

[20] W. H. Eggimann, "Higher order evaluation of electromagnetic diffraction by circular disks," *IRE Trans. Microwave Theory Tech.*, vol. MTT-9, pp. 408–418, Sept. 1961.

[21] R. E. Collin and W. H. Eggimann, "Dynamic interaction fields in a two-dimensional lattice," *IRE Trans. Microwave Theory Tech.*, vol. MTT-9, pp. 110–115, Mar. 1961.

Chryssoula A. Kyriazidou (S'98–M'99) received the B.S. degree in physics from the University of Athens, Athens, Greece in 1984, the M.S. and Ph.D. degrees in physics from The University of Michigan at Ann Arbor, in 1989 and 1992, respectively, and the Ph.D. degree in electrical engineering from the University of California at Los Angeles, in 1999.

From 1992 to 1993, she was a Post-Doctoral Research Associate with the High Energy Physics Group, Brookhaven National Laboratory. From 1993 to 1996, she was a Post-Doctoral Research Associate with Argonne National Laboratory. Her research has focused on quantum field theory with emphasis on quantum radiative corrections to electroweak scattering process. She has authored 16 publications in the area of electromagnetics. Her research interests include novel composite materials, antenna design and monolithic microwave integrated circuits (MMICs), accelerated full-wave codes for EM simulations, and modeling of propagation environments for wireless communications.

Harry F. Contopanagos (M'98) received the B.S. degree in physics from the National University of Athens, Athens, Greece, in 1984, and the M.S. and Ph.D. degrees in physics from The University of Michigan at Ann Arbor, in 1989 and 1991, respectively.

From 1991 to 1993, he was a Research Associate at the Institute for Theoretical Physics, State University of New York (SUNY) at Stony Brook, where he performed research on scattering theory in quantum electrodynamics and quantum chromodynamics. From 1993 to 1996, he was a Research Associate at Argonne National Laboratories, where he provided theoretical predictions for the production of a cross section of the newly discovered Top Quark, in excellent agreement with subsequent experiments. From 1996 to 1999, he was a Research Engineer with the Electrical Engineering Department, University of California at Los Angeles. He is currently a Senior Research Staff Scientist at HRL Laboratories, Malibu, CA. His recent researches activities include theory and fabrication of composite EM media, applications in compact high-frequency waveguide filters, printed antennas, physical modeling of communication channels, integral equations, and fast numerical implementations. He has authored 15 publications in the area of electromagnetics and 30 publications in the area of high-energy physics.

Nicólaos G. Alexópoulos (S'68–M'69–SM'82–F'87) was born in Athens, Greece, on April 14, 1942. He received the degree from the eighth Gymnasium of Athens, Athens, Greece, in 1959, and the B.S.E.E., M.S.E.E., and Ph.D. degrees from The University of Michigan at Ann Arbor, in 1965, 1967, and 1968, respectively.

From 1969 to 1996, he joined the School of Engineering and Applied Science, University of California at Los Angeles (UCLA), where he was a member of the faculty of the Electrical Engineering Department. While with UCLA, he served as Associate Dean for Faculty Affairs (1986–1987) and Chair of the Electrical Engineering Department (1987–1992). Since January 1997, he has been a Professor in the Electrical and Computer Engineering Department, University of California at Irvine, where he serves as the Dean of the School of Engineering. He has served over the years as a consultant to a variety of U.S. and foreign corporations and the U.S. Government. In addition, he has been on the editorial board of various professional journals and, more recently, he served as the Editor-in-Chief of *Electromagnetics*. He has authored over 250 refereed journal and conference proceedings papers. His recent research activities have focused on the modeling and design of three-dimensional integrated circuits and printed systems, interconnect problems in complex networks, novel materials and smart structures in low observable systems, and computational methods.

Dr. Alexópoulos was corecipient of the IEEE S. E. Schelkunoff Prize Best Paper Award in both 1985 and 1998.